Supporting Information

Vapor growth of binary and ternary phosphorus-based semiconductors into TiO_2 nanotube arrays and application in visible light driven water splitting

Ebru Üzer,[a] Pawan Kumar,[b†] Ryan Kisslinger,[b†] Piyush Kar,[b] Ujwal Kumar Thakur,[b] Karthik Shankar, [b,*] and Tom Nilges [a,*]

[a.] *Department of Chemistry, Technical University of Munich, Lichtenbergstr. 4, 85748 Garching b. München, Germany; E-mail: tom.nilges@lrz.tum.de*
[b.] *Department of Electrical and Computer Engineering, 9211-116 Street NW, Edmonton, Alberta, Canada T6G 1H9; E-mail: kshankar@ualberta.ca*
†Contributed equally

1. Experimental details

Fabrication of TiO_2 nanotube membranes

TiO_2 nanotube membranes were fabricated through anodization.[1] Titanium foil was used as both the anode and cathode; the anode was 4 cm long and 1 cm wide, while the cathode was 2 cm long and 0.5 cm wide. Both the cathode and anode were 0.89 mm thick. The electrolyte was comprised of 97:3 v/v ethylene glycol and deionized water, with 0.03 wt.% NH_4F added in. The electrolyte was stirred vigorously before anodization. The anode and cathode were spaced 2 cm in the solution, and the 100 mL beaker containing the electrolyte submerged in a water bath for cooling. A voltage of 60 V was applied for 3 d to create the nanotube arrays; they were then dipped in methanol for cleaning, and the 0.89 mm thick sides of the anodized pieces scratched off with a razor to allow them to delaminate during subsequent air drying. To open the bottoms of the nanotubes and clean the tops of any debris, the delaminated nanotube arrays (membranes) were subjected to reactive ion etching using Oxford PlasmaPro NGP80. An SF_6 etch using a pressure of 20 mTorr and a forward power of 250 W was used for 200 s on the top and 300 s on the bottom (see Results and Discussion for explanation of our top versus bottom terminology). An oxygen cleaning using a pressure of 150 mTorr and a forward power of 225 W for 10 min was used on each side.

Synthesis of hybrid NaP_x@TiO_2 nanotube membranes

The chemical vapour deposition of NaP_7 and NaP_{15} on TiO_2 nanotube membranes was synthesized according to literature procedures.[2] A mixture of the elements sodium and red phosphorus in the atomic ratio of 1:7 was prepared by transferring red Phosphorus (452.1 mg, 99.999+%, Chempur) and Sodium (47.9 mg, 99,95% in oil, Aldrich) into a silica-glass tube (0.8 cm inner diameter, 8 cm length). Into the previously graphitized glass tube, purified CuI (10 mg) together with TiO_2 nanotube membranes was added. The ampoule was sealed under vacuum ($p < 10^{-3}$ mbar) and placed horizontally in the chamber of a muffle furnace to obtain a temperature gradient of approx. 10 K. By locating the starting materials in the hot zone of a Nabertherm muffle furnace (L3/11/330) and TiO_2 nanotube membranes in the colder zone, a dissolution *via* gas phase and deposition on the TiO_2 nanotube membranes was attempted. The furnace was set to 823 K within 10 h and held at this temperature for 7 d. The products were formed after cooling down by switching off the furnace. Deposition of thin red-brown fibres on the TiO_2 nanotube arrays were observed. Red, block-like crystals of NaP_7 were formed simultaneously.
Purification of the mineralizer CuI was carried out by solving CuI (98+%, Chempur) in concentrated HI (57 %, Riedel de Häen) and following precipitation in water. The precipitate was purified by washing twice with water and ethanol and subsequently dried under vacuum.

Synthesis of hybrid SnIP@TiO_2 nanotube membranes

The preparation of hybrid SnIP@TiO_2 nanotube membranes was carried out following the bulk-SnIP literature procedure.[3] The starting materials Sn (107.8 mg, 99,999%, Chempur), SnI_4 (189.6 mg, synthesized according to literature procedures),[4] and red phosphorus (37.5 mg, 99.999+%, Chempur) were pressed into a pellet (diameter: 10 mm, 25 MPa for 15 min). The pellet and TiO_2 nanotube membranes were transferred into a silica glass tube, the ampoule was sealed under vacuum ($p < 10^{-3}$ mbar) and placed horizontally in a Nabertherm muffle furnace (L3/11/330). The materials were located at the hot zone at 923 K and the membranes at the colder zone of the furnace. Cooling the melt down to 773 K within 15 h at a rate of 2 K h^{-1} and of 1 K h^{-1} to room temperature led to deposition of SnIP onto the TiO_2 nanotube membranes.

Synthesis of $(CuI)_3P_{12}$@TiO_2 nanotube membranes

The synthesis of $(CuI)_3P_{12}$@TiO_2 nanotube membranes was attained according to literature procedures.[5] Purified CuI (181.8 mg) and red Phosphorus (118.2 mg, 99.999+%, Chempur) were pressed into a pellet (diameter 10 mm, 25 MPa for 15 min). The pellet was placed in a silica glass tube (0.8 cm inner diameter, 8 cm length) with TiO_2 nanotube membranes, located at the opposite side. The ampoule was sealed under vacuum ($p < 10^{-3}$ mbar) and laid horizontally in a Nabertherm muffle furnace (L3/11/330) so that the starting materials are located at the hot zone of the furnace and the TiO_2 nanotube membranes at the colder zone. The furnace was heated to 773 K within 8 h, with a holding period of 48 h, cooled down to 673 K within 24 h and held at this temperature for 11 d. Room temperature was reached within 24 h.
CuI was purified as it was mentioned in a previous paragraph.

Synthesis of polyphosphide@TiO_2 nanotube hybrids

TiO_2 nanotube membranes were prepared by electrochemical anodization of titanium foil to produce an ordered array of parallel-aligned TiO_2 nanotubes. The membranes had two distinct sides: a side that was exposed to the electrolyte during the anodization process (top side) and a side that was delaminated from the underlying titanium substrate (bottom side). Owing to the fluoride etching process during anodization, the top side had thinner sidewalls and thus large inner tube diameter. The nanotube bottoms had an average inner diameter of 67±9 nm (n = 50 nanotubes), shown in Figure 1b; the nanotube tops had an average inner diameter of 120±13 nm (n = 50 nanotubes), shown in Figure 1c. To maximize the probability of deposition inside of the tubes, the nanotubes were placed top side up in the ampoule. To fabricate hybrid semiconducting materials, we succeeded in filling the anatase-type TiO_2 nanotubes with binary NaP_7/NaP_{15}, and ternary $(CuI)_3P_{12}$, SnIP using a short-way transport reaction; this reaction is adapted from the so-called mineralization-principle used for the synthesis of a plethora of phosphorus-containing compounds. Notably, owing to the TiO_2 nanotube structure necessary to deposit sodium polyphosphides on and inside the membranes, the structure withstood the thermal treatment and led to deposition of respective polyphosphides onto and into the membranes.

1.1 Physicochemical characterization

X-ray powder diffraction

X-ray powder data were collected on a Stoe STADI P diffractometer (Cu-$K_{\alpha1}$ radiation, λ = 1.54060 Å, Ge-monochromator) fitted with a Mythen 1 K detector (Fa. Dectris). An external calibration was performed using a silicon standard (a = 5.43088 Å). Phase analysis and indexing was carried out with the program package Stoe WinXPOW.[6]

Scanning Electron Microscopy (SEM) and Energy Dispersive X-ray spectroscopy (EDS).

TiO_2 nanotubes and according nanofibers were investigated *via* Scanning Electron Microscopy with a SEM JCM-6000 NeoScop TM (JEOL, 5900LV, Si(Li) detector). The compositions of the hybrid compounds were determined semi-quantitatively by EDS measurements (Energy Dispersive X-ray Spectroscopy, Röntec). The samples were applied with an acceleration voltage of 15 kV. The measured composition is in good agreement with the composition achieved from structure refinement.

Scanning Transmission Electron Microscope (STEM) and Energy Dispersive X-ray spectroscopy (EDS).

STEM-EDS analysis was performed on a JEOL JEM-ARM200cF STEM, which is equipped with a cold Field-Emission Gun (cFEG) and a probe Cs corrector. EDS maps were acquired with a Silicon Drift (SDD) EDS detector at an acceleration voltage of 200 kV.

Helium Ion Microscope (with Ga-FIB)

For SEM and Auger analysis, samples were prepared using a Zeiss ORION NanoFab Helium Ion Microscope, equipped with a Ga-FIB column. The cross section of TiO_2 nanotubes was milled and polished with a 30 keV Ga-FIB at beam currents of 1.5 nA.

Raman spectroscopy

Raman studies were performed at 300 K by using a Renishaw inVia RE04 Raman Microscope fitted with a Nd:YAG laser (λ = 532 nm) and a CCD detector. A laser power of 250 mW was applied recording a total number of 500 scans.

Auger electron spectroscopy

SEM and Auger measurements were performed using a JAMP-9500F Auger microprobe (JEOL) at the Alberta Centre for Surface Engineering and Science, University of Alberta. A Schottky Field emitter was used to generate an electron probe diameter of about 3 to 8 nm at the sample. Sample cleaning was conducted using argon ion sputtering, over an area of 500 μm^2 with a sputtering rate of 15 nm/min as calibrated using SiO_2. The SEM and Auger imaging were performed at an accelerating voltage of 2 kV and emission current of 20 mA. The working distance used was 24 mm. The sample was rotated 30 degrees away from the primary electron beam to face the electron energy analyzer. For the Auger spectroscopy and imaging a M5 lens with 0.6 % energy resolution was applied.

X-ray Photoelectron spectroscopy (XPS) and ultraviolet photoelectron spectroscopy (UPS)

The surface chemical composition and oxidation state of materials was determined with X-ray photoelectron spectroscopy (XPS) by using Axis-Ultra, Kratos Analytical instrument equipped with monochromatic Al-Kα source (15 kV, 50 W) and photon energy of 1486.7 eV under ultra-high vacuum (UHV $\sim 10^{-8}$ Torr). The binding energy of C1s of adventitious hydrocarbon (BE ≈ 284.8 eV) was used as standard to assign binding energy (BE) of other elements by carbon correction. The obtained raw data was deconvoluted in various peak components using CasaXPS and acquired .csv file were plotted using origin 8.5. To determine the band structure of materials the work function spectra and valence band spectra of materials were determined by using ultraviolet photoemission spectroscopy (UPS) with Axis-Ultra, Kratos Analytical instrument and He I line (21.21 eV) of He discharge lamp source.
Additionally, valence band position of bare TiO_2 nanotubes was determined with XPS valence band spectra acquired on Axis-Ultra, Kratos Analytical instrument under ultrahigh vacuum conditions.

Diffuse reflectance UV-Vis (DR-UV-Vis)

Diffuse reflectance UV-Vis spectra to determine UV-Vis absorption profile of materials was acquired on a Perkin Elmer Lambda-1050 UV–Vis-NIR spectrophotometer equipped with an integrating sphere accessory.

Kelvin Probe Force Microscopy (KPFM)

To discern the charge separation dynamics and validate formation of heterojunction between polyphosphides and TiO_2, the surface potential (SP) or contact potential difference (CPD) of materials was measured using peak force KPFM (Kelvin probe force microscopy) using Dimension Fast Scan Atomic Force microscope (Bruker Nanoscience Division, Santa Barbara, CA, USA). For measurements, the materials were deposited on FTO, and a Pt-coated SiNSCM-PIT cantilever of 2.5 4.4 N/m stiffness was employed to perform the KPFM experiments. Samples were grounded with the AFM chuck with the help of conductive copper tape. The measurement was performed at zero tip bias and Pt tip was calibrated by measuring the CPD of HOPG and the Pt tip using following expression:
EF (tip) = 4.6 eV (Work function of HOPG) + VCPD (HOPG and Pt tip)

1.2 Electrochemical characterization

Analytical grade KOH (99.0%), anhydrous Na_2SO_4 (99.0%), titanium (IV)-isopropoxide (99.99%), were procured from Sigma Aldrich and used without any further purification. Conductive Fluorine doped tin oxide (FTO) glass (transmittance 80-82%) was purchased from Hartford Tec Glass Company. The surface of FTO was cleaned by ultrasonication in water, methanol and acetone for 10 min to remove any residual organics. All the solvent/water used in the measurements were of HPLC grade.

Photo-electrochemical measurements

The electrochemical properties of the materials were determined by using a CHI660E series electrochemical workstation in a three-electrode configuration. The photoactive materials deposited on FTO glass containing a TiO_2 blocking layer was assigned as anode (working electrode), while Pt sputtered glass and Ag/AgCl was used as cathode (counter electrode) and as reference electrode respectively. To ensure an equal amount of photocatalytic materials on the photoanodes, an identical amount of materials, dispersed in methanolic solution was drop-casted on the exact same area of TiO_2 seed layer containing FTO glass. The photoelectrochemical measurements were performed in 0.1 M KOH aqueous electrolyte. Linear sweep voltammetry (LSV) to measure the materials photocurrent density was performed by sweeping voltage from –1.0 V to +0.8 V vs Ag/AgCl at a scan rate of 10 mV/sec. The photoanode was irradiated with solar simulated light (AM1.5 G) having a power density of 100 mW m^{-2} at the sample surface by using Newport, Oriel instrument USA, model 67005, solar simulator. To determine visible light response at higher wavelengths and incident photon-to-current efficiency (IPCE) the samples were irradiated with monochromatic 450 and 505 nm wavelength LEDs having 54.15 and 40.48 mW cm^{-2} incident power density at the sample surface. Mott-Schottky plots to calculate flat band potential were extracted from impedance-potential values measure in 0.5 M Na_2SO_4 solution in a potential range of –1.0 to +1.0 V at 1 K frequency. Electrochemical impedance spectroscopy (EIS) to draw Nyquist plots and equivalent circuit under dark and 1 Sun irradiation was performed using a three

electrodes configuration at a bias of –0.5 V vs Ag/AgCl in 0.1 M KOH, with an AC amplitude of 0.005 V at frequency value 1 Hz - 100 kHz.

To investigate the photo-electrochemical performance an approx. 20 nm thick TiO_2 blocking layer was spin casted on cleaned FTO glass using titanium isopropoxide solution according to our previous report just by changing the dilution of the solution three times.[6] The deposition of photoactive materials on TiO_2 coated FTO was done by dispersing materials in very dilute aqueous solution of titanium isopropoxide and drop casting followed by heating at approx. 150 ºC for 1 h. In this way the materials stick strongly on the TiO_2 coated FTO substrate. The materials deposited on FTO glass function as photoanode (working electrode) and Pt and Ag/AgCl was used as counter (cathode) and reference electrodes, respectively. The photo-electrochemical water splitting experiments were performed by immersing the electrodes in 0.1 M KOH solution. The samples were irradiated under solar simulated light (AM1.5 G) having a power density of 100 mW cm^{-2} at the sample surface and photocurrent density was measured in function of applied voltage by sweeping bias from –1.0 V to +0.8 V. Further, photocurrent response at higher wavelength (monochromatic 450 and 505 nm light) was measured using LEDs and with power density on the sample surface was 54.15 and 40.48 mW cm^{-2}.

2. Results

NaP_7@TiO_2 nanotubes

P-XRD analysis

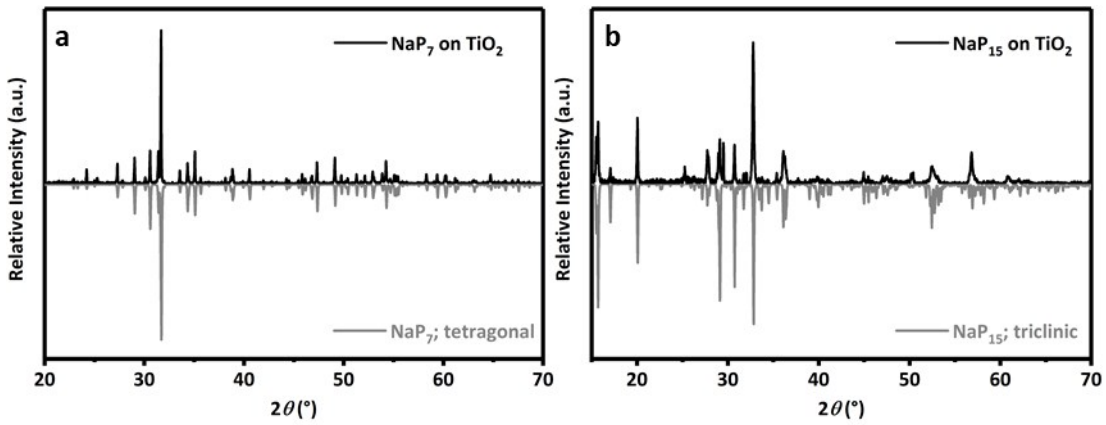

Figure S1. a) and **b)** Powder X-ray diffraction patterns of NaP_7 (main fraction) and NaP_{15} (minor fraction) substantiate the formation of the two polyphosphides on the membrane.

AES analysis

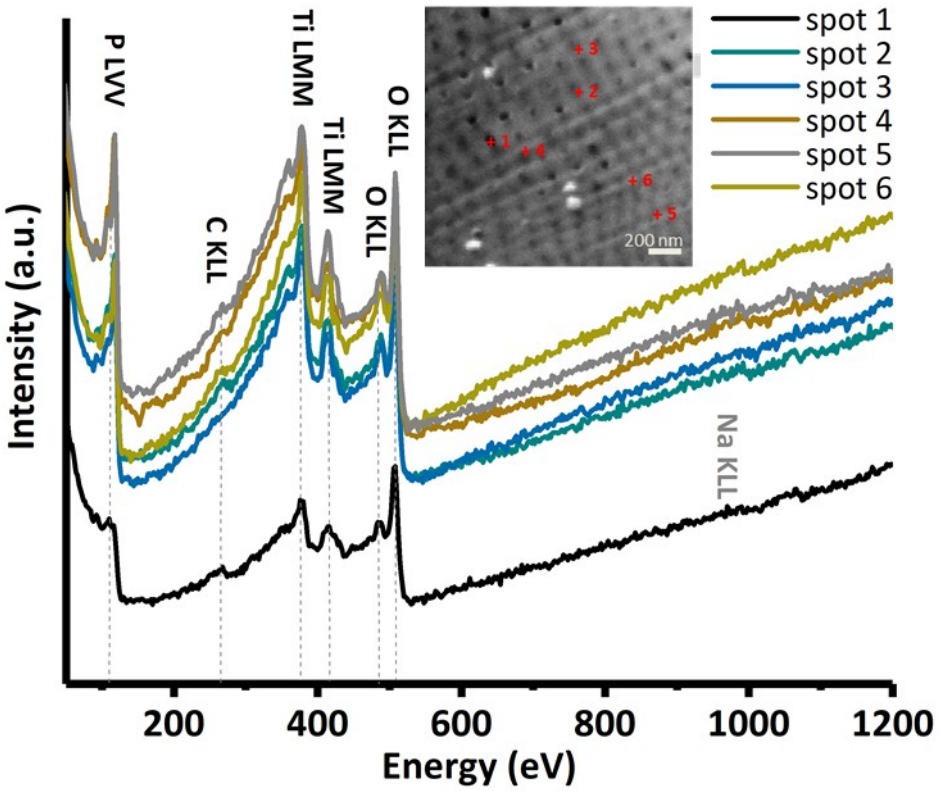

Figure S2. Selected point AES spectra on FIB-milled NaP_x@TiO_2 nanotube specimen. The according peaks at spot 1 (seeming hole) are P LVV (115 eV), C KLL (266 eV), Ti LMM (381 eV, 416 eV), O KLL (482 eV, 503 eV), a weak peak at 979 eV potentially caused by Na KLL.

SnIP@TiO_2 nanotubes

P-XRD analysis

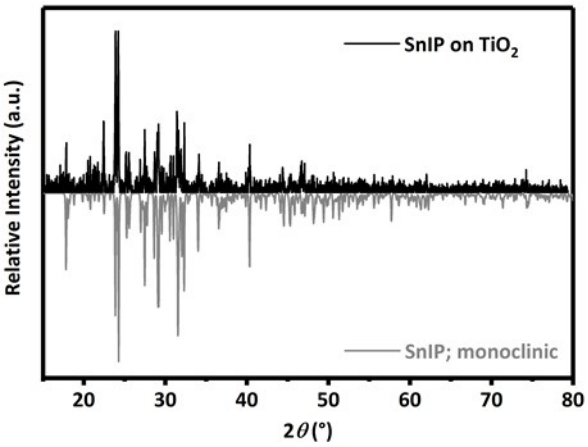

Figure S3. Powder X-ray diffraction patterns confirm the formation of crystalline SnIP onto the membrane.

$(CuI)_3P_{12}$@TiO_2 nanotubes

The gas-phase based synthesis was furthermore applied for the ternary polyphosphide $(CuI)_3P_{12}$. According to calculations $(CuI)_3P_{12}$ and its structurally related compounds $Cu_2I_3P_3$, and $(CuI)_2P_{14}$ show a band gap range of 1.0 - 1.1 eV.[7] Downsizing quantum confinement effects such as in single and isolated phosphorus ${}^{1}_{\infty}[P10]P2[$ strands without the CuI-matrix lead to bandgaps of 2.3 - 2.9 eV.[7] A growth of such isolated strands can be achieved by the infiltration in hollow TiO_2 nanotubes.

The polyphosphide substructure consists of condensed five- and six-membered ring fragments attached to a polymer subunit in the CuI matrix.[5] In line with Baudler's rules the one-dimensional infinite phosphorus chains ${}^{1}_{\infty}([P10]P2[)^{0}$ in the $(CuI)_3P_{12}$ structure are more stable than the structurally related $Cu_2I_3P_3$ with infinite chains ${}^{1}_{\infty}[P^{0}_{12}]$ inhibiting additional four-membered rings.[8-11] In Figure S4a the $(CuI)_3P_{12}$ - crystal structure consisting of separated CuI and polymeric phosphorus tubes along the b-axis is demonstrated. A microscopic image of the TiO_2 nanotube membranes show the surface covered with dark blue fibres of $(CuI)_3P_{12}$ (Figure S4b). The SEM image in Figure S4c confirms preservation of the nanotube structure after gas phase synthesis procedure as well as the according elemental composition (Table S3). Powder X-ray diffraction verifies the growth of $(CuI)_3P_{12}$ on top of the TiO_2 nanotube membranes (Figure S4d).

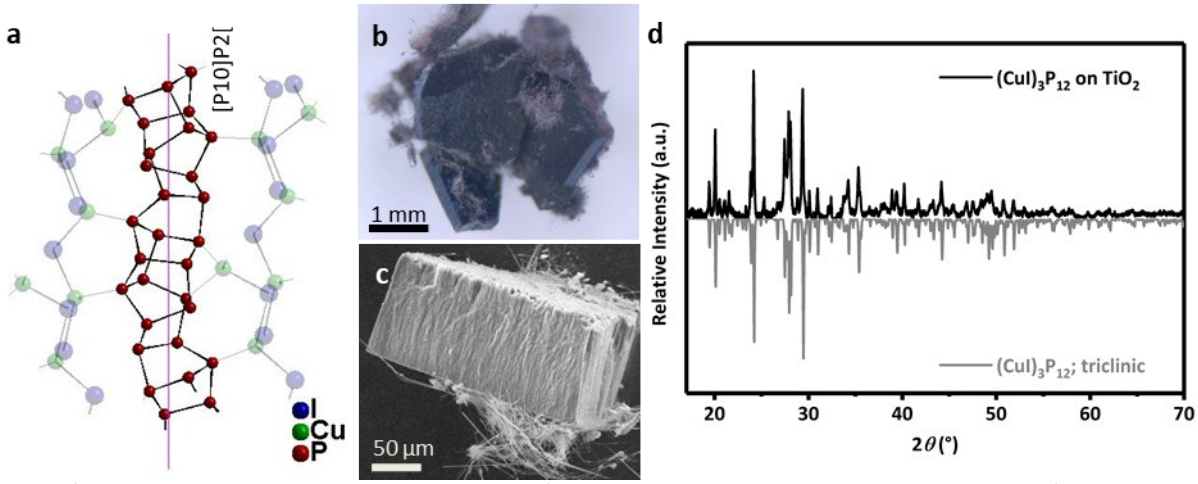

Figure S4. **a)** Crystal structure of $(CuI)_3P_{12}$ with CuI and polymeric P units. **b)** A TiO_2 nanotube membrane reacted with $(CuI)_3P_{12}$ *via* gas phase. **c)** Cross section and surface of $(CuI)_3P_{12}$@TiO_2 nanotube membranes. **d)** Powder X-ray diffraction patterns confirm the formation of crystalline $(CuI)_3P_{12}$ onto the membrane.

Raman imaging of the razor-cut cross section of hybrid $(CuI)_3P_{12}$@TiO_2 nanotube membranes cutting demonstrates the successful growth of $(CuI)_3P_{12}$ crystals up to 22 µm in distance to the membrane-top side (Figure S5).

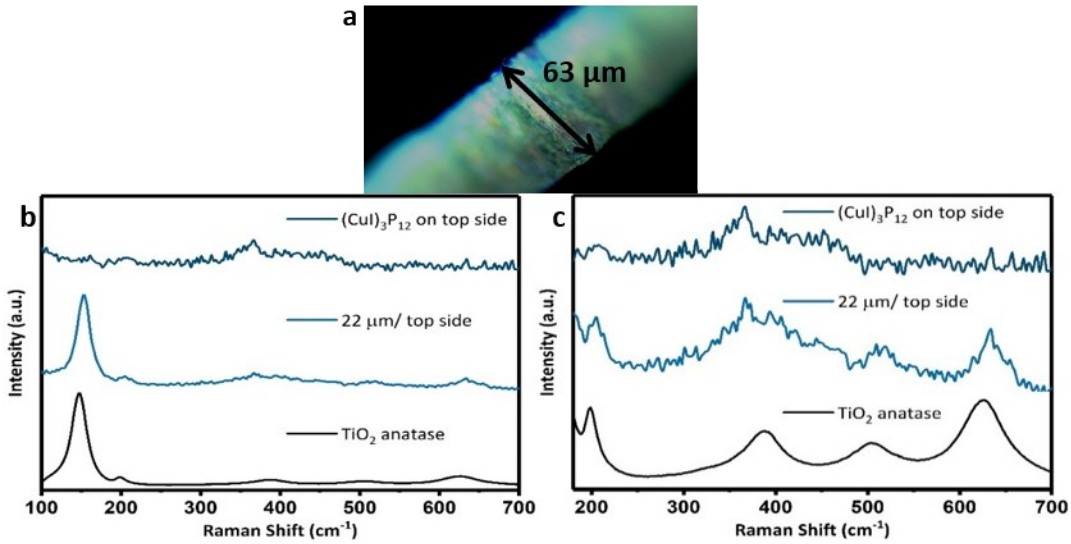

Figure S5. Raman spectroscopy on $(CuI)_3P_{12}@TiO_2$ membranes. **a)** Corresponding membrane cross section of measured specimen. **b)** From top to down: Reference Raman spectrum of measured $(CuI)_3P_{12}$ crystals, spectra of a $(CuI)_3P_{12}@TiO_2$ membrane cross section measured at approx. 22 µm in distance to the surface (membrane-top side and a fresh TiO_2 membrane (anatase, grey). **c)** A zoom in into the significant bands between 300 and 550 cm-1 of the $(CuI)_3P_{12}$ Raman spectrum.

STEM images show a ranged bundle of non-decayed TiO_2 nanotubes taken after separation by an ultrasonication process. The image scale displays a size of ~90-100 nm per tube. An infiltration is shown by distribution of Ti and P along, with Cu and I according to elemental mapping is illustrated along the tube length of the nanotube bundle (see Figure S6a).

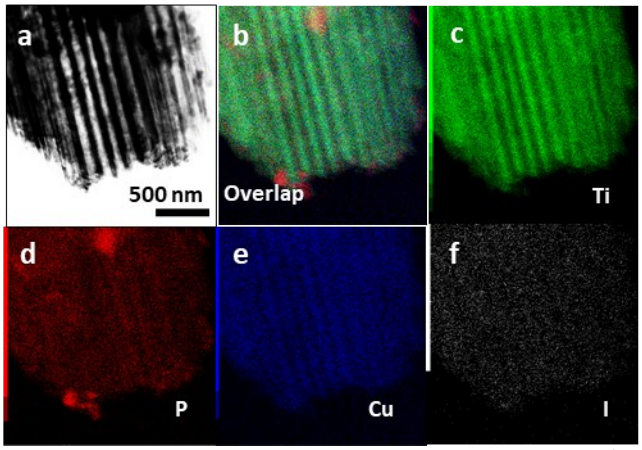

Figure S6. a) STEM bright-field image of TiO_2 nanotubes separated from a membrane by an ultrasonication procedure. **b)** Elemental mapping of overlaid elements Ti (representing TiO_2), P, Cu and I. The elemental mapping images of **c)** Ti, d) P, e) Cu and f) I substantiating P, Cu and I distributed along the length of a TiO_2 nanotube bundle.

XPS analysis

High resolution X-ray photoelectron spectroscopy (HR-XPS) was performed to investigate the surface chemical composition, binding energy and oxidation state of the elements. XPS elemental survey scan of NaP_7, TiO_2 and $NaP_7@TiO_2$ reveals the presence of all elements in NaP_7 (Na1s, P2p), TiO_2 (Ti2p, O1s) and $NaP_7@TiO_2$ (Na1s, P2p, Ti2p, O1s) (Figure S7a). HR-XPS in Ti2p region for TiO_2 reveal two peak components at BE ≈ 459.46 and 465.27 eV assigned to $Ti2P_{3/2}$ and $Ti2p_{1/2}$ splitting, demonstrating presence of anatase form TiO_2 with Ti^{4+} in crystal lattice (Figure S7b).[12] The peak position of $Ti2P_{3/2}$ and $Ti2p_{1/2}$ components does not change in hybrid $NaP_7@TiO_2$ suggesting anatase phase TiO_2 remains intact during deposition step. The deconvoluted HR-XPS spectra of TiO_2 nanotubes in O1s region shows two peak components at 530.98 and 532.70 eV. The strong peak at 530.98 eV was originated from lattice oxygens bonded to Ti in crystal (Ti-O-Ti), while relatively weak shoulder peak at 532.70 eV was assigned to non-lattice adventitious oxygen and surface –OH groups. Additionally, two peak components in O1s spectra cantered at 530.98 and 532.70 eV for TiO_2 remains unchanged in and $NaP_7@TiO_2$ which reveal robust nanotube

structure even after vapor phase deposition of NaP_7 on TiO_2 (Figure S7c).[13] However, the increase in peak intensity of 532.70 eV exhibit increase in adventitious oxygen which might be due to partial surface oxidation of phosphide to various P-O moieties (P_xO_y). The peak positioned at 1063.74 eV in Na1s HR-XPS spectra for NaP_7 originated from electrostatically bonded Na^+ to the phosphide backbone.[14-17] Surprisingly, The Na1s peak in NaP_7@TiO_2 was shifted to higher binding energy which might be due to partial charge transfer from NaP_7 to the surface of TiO_2 and partial doping of TiO_2 surface with Na ions (Figure S7d). Additionally, HR-XPS of NaP_7 in P 2p region show two peaks centred at BE ≈ 130.15 and 134.16 eV. The peak at 129.86 eV can be further deconvoluted into two peak components located at BE≈129.90 and 130.77 eV and might have originated due to coexistence of two phases NaP_7 (dominant fraction) and NaP_{15} (both responsible for the 129.86 eV peak due to comparable polyphosphide substructures and crystallographically non-equivalent P species)[16, 17] The peak at 134.16 eV was originated due to partially oxidized surfaces (phosphate formation, P_xO_y). A significant increase of the peak positioned at 130.15 eV appears in the NaP_7@TiO_2 nanocomposite. The increase signal intensity might be due to a reduced oxidation tendency of the polyphosphide in the hybrid (Figure S7e).

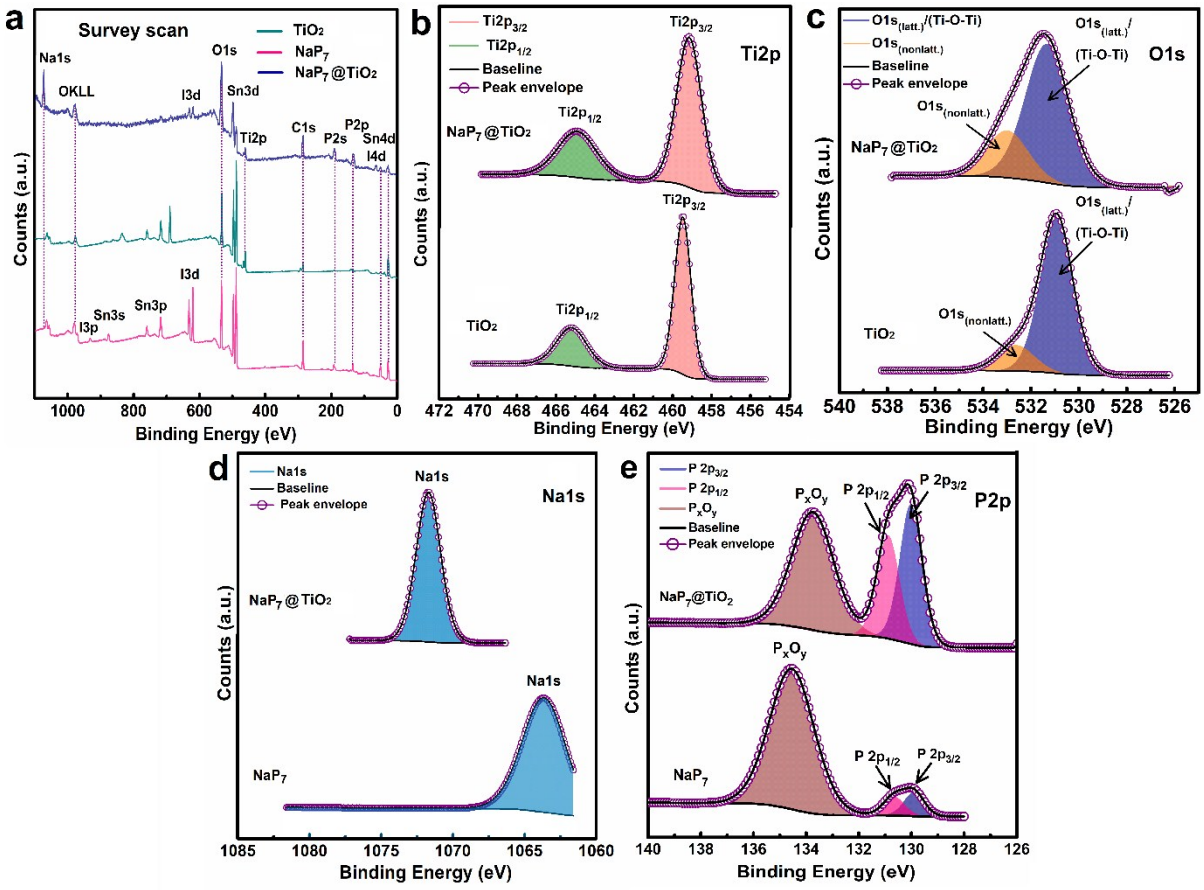

Figure S7. a) Elemental survey scan of TiO_2 nanotube membranes (green), NaP_7 (pink) and NaP_7@TiO_2 (navy blue) and HR-XPS spectra of TiO_2 and NaP_7@TiO_2, **b)** in Ti2p region, **c)** in O1s region, **d)** in Na1s region, **e)** in P2p region.

Like NaP_7, the elemental survey scan of $(CuI)_3P_{12}$, TiO_2 nanotube membrane and hybrid $(CuI)_3P_{12}$@TiO_2 confirms presence of all the relevant elements in $(CuI)_3P_{12}$ (Cu, I and P), TiO_2 and $(CuI)_3P_{12}$@TiO_2 (Cu, I, P, Ti and O) (Figure S8a). The high resolution XPS (HR-XPS) core level spectra of TiO_2 in Ti2p region can be deconvoluted into two peak components located at binding energy 459.46 and 465.27 eV assigned to $Ti2p_{3/2}$ and $Ti2p_{1/2}$ components of Ti^{4+} oxidation state of anatase phase TiO_2 (Figure S8b).[18, 19] After solid state vapour phase deposition of $(CuI)_3P_{12}$ on TiO_2 nanotube membranes ($(CuI)_3P_{12}$@TiO_2) the binding energy of $Ti2p_{3/2}$ and $Ti2p_{1/2}$ components doesn't change, which confirms that the chemical nature of TiO_2 doesn't change during deposition of $(CuI)_3P_{12}$. The HR-XPS spectra of TiO_2 in O1s region can be deconvoluted into two peak components at 530.48 and 532.64 eV. The origin of the stronger peak at BE ≈ 530.48 eV was attributed to lattice oxygens (Ti-O-Ti), while smaller peak component located at 532.68 eV was originated due to presence of non-lattice adventitious oxygen and surface –OH groups (Figure S8c).[20] For $(CuI)_3P_{12}$@TiO_2, the binding energy of O1s peak components corresponding to lattice oxygen and adventitious oxygens remains identical; however, the intensity of non-lattice bounded peak components are increased significantly which might be due to the affinity of $(CuI)_3P_{12}$ to moisture and oxidation of surface phosphorous to

phosphates (P_xO_y). HR-XPS spectra of bare $(CuI)_3P_{12}$ in Cu2p region displayed two peak components at BE ≈ 932.91 eV and 952.55 eV, attributed to $Cu2p_{3/2}$ and $Cu2p_{1/2}$ components of Cu present in the +1 oxidation state (Figure S8d).[21, 22] Furthermore, the absence of any shoulder peak in Cu2p XPS at higher binding energies confirms the presence of Cu^{1+} atoms in identical chemical environment.[23] The Cu2p HR-XPS remains the same for the hybrid of $(CuI)_3P_{12}@TiO_2$, which demonstrates successful solid-state deposition of $(CuI)_3P_{12}$ on TiO_2 nanotubes. Two peak components in HR-XPS scan in I3d region corresponded to $I3d_{5/2}$ and $I3d_{3/2}$ at BE of 631.42 and 619.94 eV show a presence of I^- coordinated to Cu^{1+} composing Cu-I-Cu bridges of polymeric structure (Figure S8e).[24, 25] The binding energy of the I3d peak component in $(CuI)_3P_{12}@TiO_2$ gets shifted slightly to higher binding energy which might be due to chemical interaction of outer coordinated iodine with electronegative oxygen of TiO_2. Additionally, the single peak component in P2p region (134.95 eV) of $(CuI)_3P_{12}$ might be originated due contribution from oxidized P atoms present in the form of phosphate (P_xO_y) and the presence single phase Cu and iodine bonded phosphide chain (Figure S8f).[26, 27] However, considering high signal intensity we inferred phosphides were main contributor to this signal. Further the peak located at 134.95 eV can be split into two peak components centred at 134.39 and 135.27 eV for $2p_{3/2}$ and $2p_{1/2}$ peak components. Similar to the I3d peak, the P2p peak component gets shifted to higher binding energies due to the slight charge transfer from phosphorous helix to TiO_2 surface.

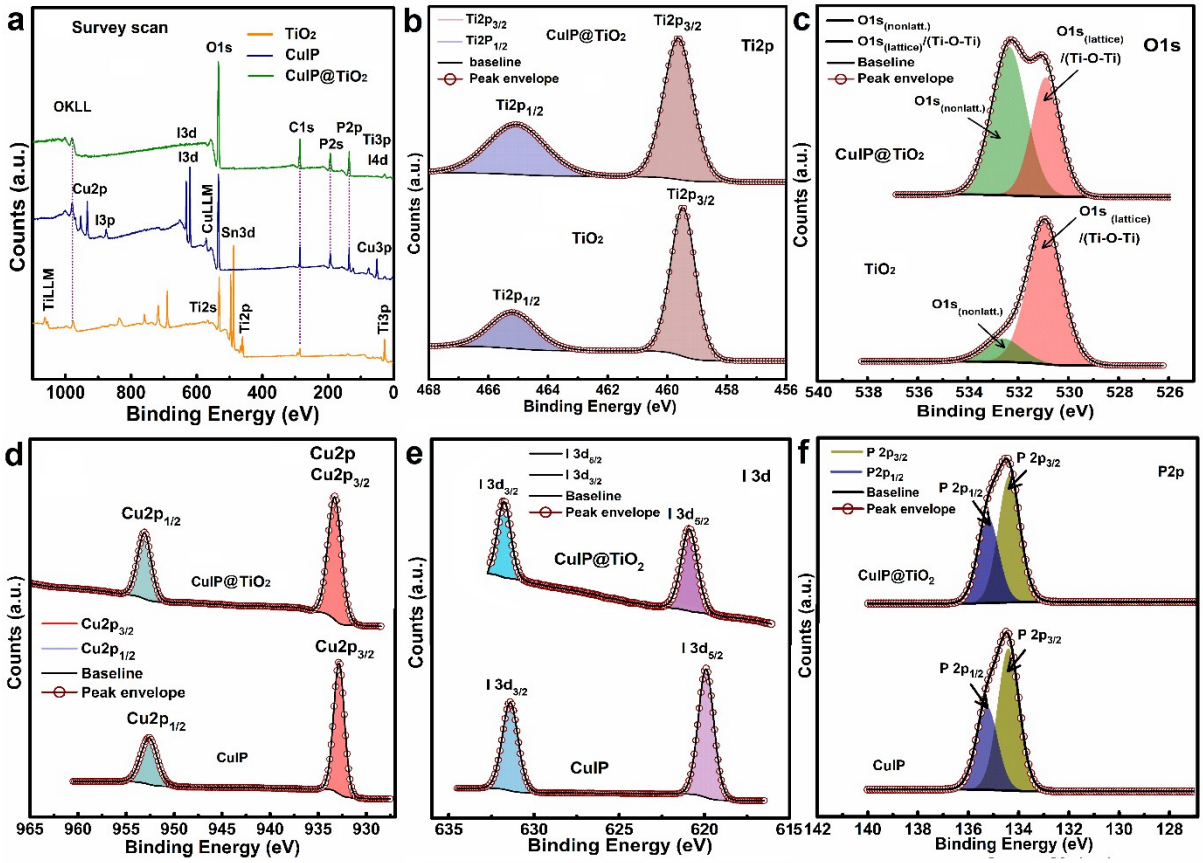

Figure S8. a) Elemental survey scan of TiO_2 nanotube membranes (orange), $(CuI)_3P_{12}$ (navy blue) and $(CuI)_3P_{12}@TiO_2$ (green), HR-XPS core level spectra of TiO_2 and $(CuI)_3P_{12}@TiO_2$, **b)** in Ti2p region, **c)** in O1s region, and HR-XPS spectra of $(CuI)_3P_{12}$ and $(CuI)_3P_{12}@TiO_2$ **d)** in Cu2p region, **e)** in I3d region and **f)** in P2p region. (CuIP ⇒ $(CuI)_{12}P_3$).

The elemental survey scan of SnIP, TiO_2 and $SnIP@TiO_2$ displayed all peaks of composing elements present in SnIP (Sn3d, I3d, P2p), TiO_2 (Ti2p, O1s) and $SnIP@TiO_2$ (Sn3d, I3d, P2p, Ti2p, O1s) (Figure S9a). The HR-XPS spectra of the bare SnIP samples in Sn3d region displayed two deconvoluted peaks at 487.51 and 495.88 eV attributed to $Sn3d_{5/2}$ and $Sn3d_{3/2}$ components, revealing a presence of chemically equivalent Sn present in +2 oxidation state (Figure S9b).[28, 29] The HR-XPS spectra of SnIP showed two peak components at binding energies 619.87 and 631.37 eV in I3d region assigned to $I3d_{5/2}$ and $I3d_{3/2}$ peak component of I- composing the SnIP helix (Figure S9c).[30, 31] Additionally, HR-XPS spectra of SnIP in P2p region show two peaks at 134.01 eV (deconvoluted into two components, $2p_{3/2}$-133.73 eV and $2p_{1/2}$-134.71 eV) for crystallographic non-equivalent P of SnIP and 139.77 eV (Phosphate, surface oxidation product P_xO_y) (Figure S9d).[32, 33] The binding energies corresponding to Sn2p, I3d and P2p peak components remain fairly constant after fabrication of SnIP on TiO_2 ($SnIP@TiO_2$) which signify the absence of any chemical interaction between SnIP and TiO_2 (Figure S9b-d). The HR-XPS core level spectra in Ti2p region for TiO_2

nanotubes displays two peak components at 466.43 and 465.23 eV assigned to $Ti2p_{3/2}$ and $Ti2p_{1/2}$, revealing the Ti^{4+} states in anatase TiO_2 lattice (Figure S9e).[34] The HR-XPS spectra in O1s region of TiO_2 deconvoluted into two peak components gave peak at BE≈ 531.86 and 532.74 eV corresponding to lattice bounded oxygen and adventitious surface adsorbed oxygen (Figure S9f).[35] After gas-phase deposition of SnIP on TiO_2 nanotube membranes the signal for Ti2p disappeared which was assumed due to coverage of TiO_2 nanotube membrane with SnIP materials resulting in suppression of the signals at the measured area (Figure S9e). While the O1s signal get slightly shifted to lower binding energies (530.98 eV) and the peak component at 532.74 eV gets increased, showing some oxidation of SnIP phosphorus to P-O (P_xO_y) functionalities and surface adsorbed adventitious oxygen.[36]

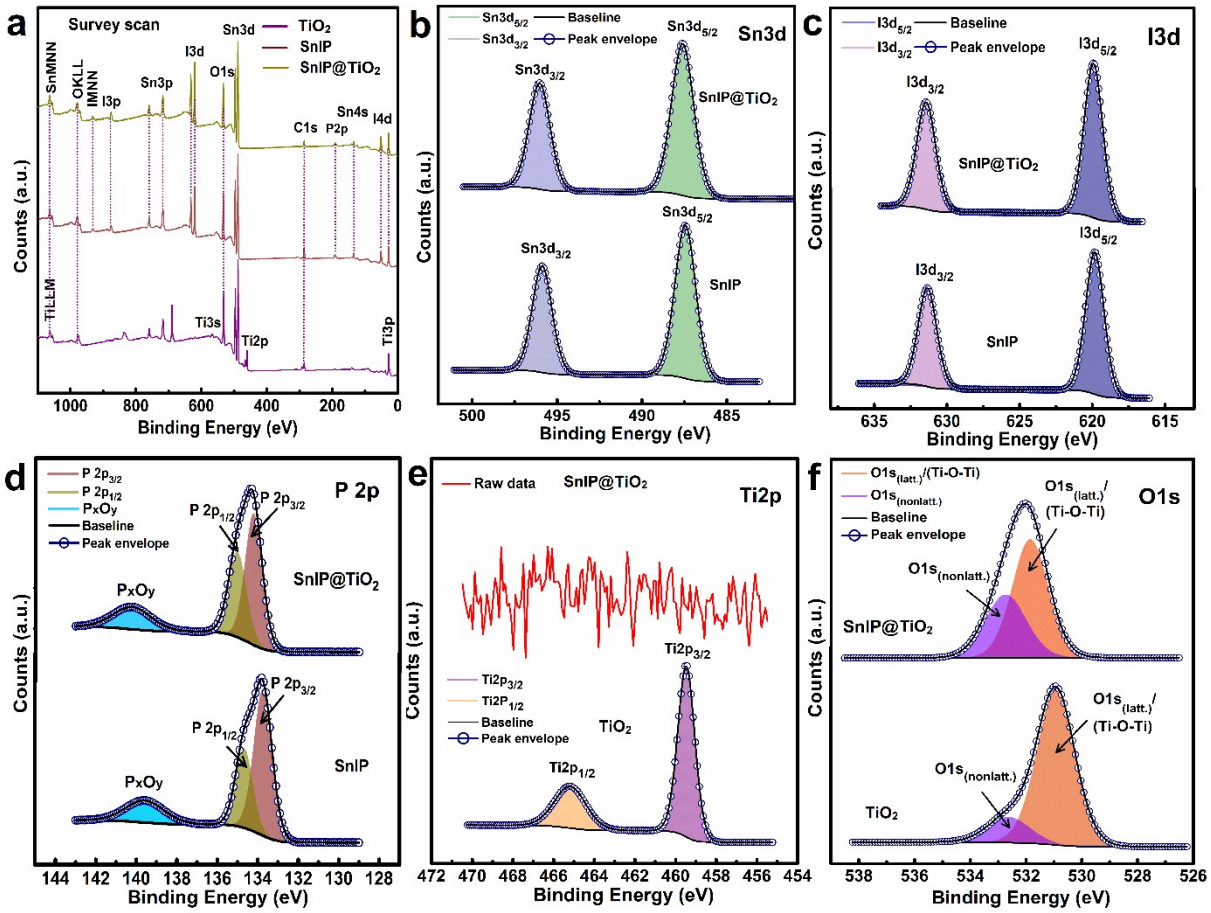

Figure S9. a) Elemental survey scan of TiO_2 nanotube membranes (purple), SnIP (red) and SnIP@TiO_2 (yellow) and HR-XPS core level spectra of TiO_2 and SnIP@TiO_2, **b)** in Sn3d region, **c)** in I3d region, **d)** in P2p region, **e)** in Ti2p region and **f)** in O1s region.

Diffuse reflectance spectroscopy

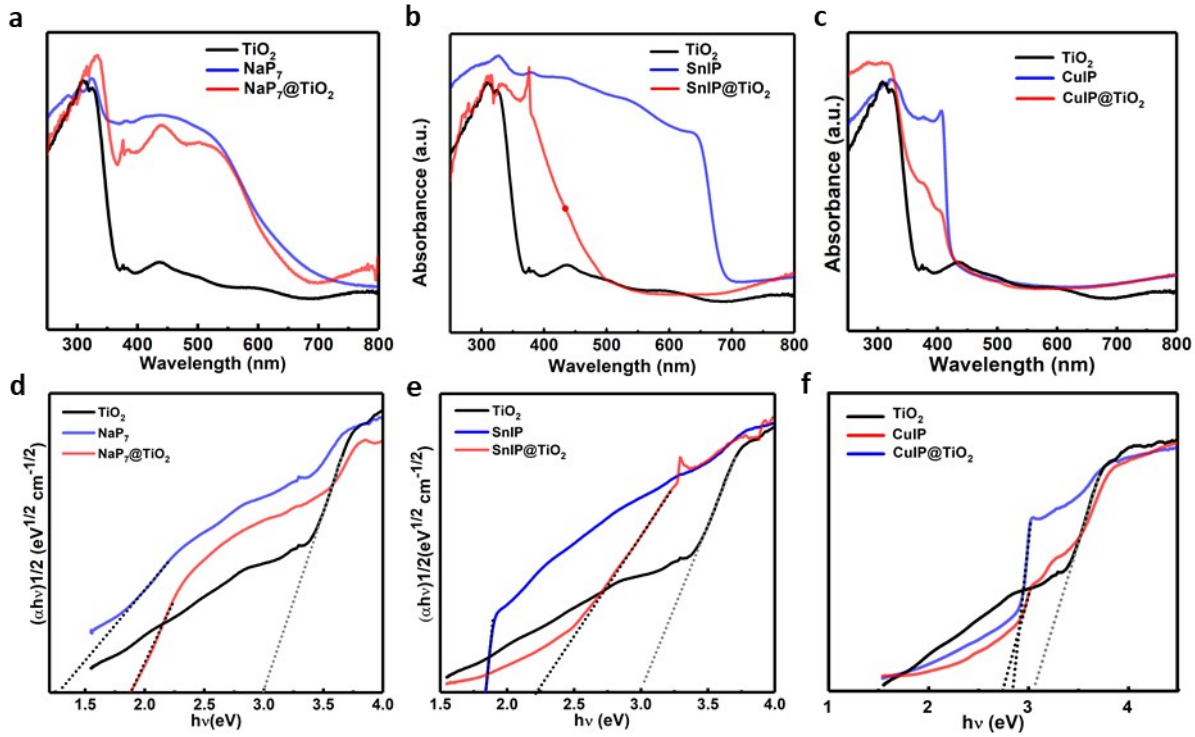

Figure S10. UV-Vis DRS spectra of **a)** TiO_2 nanotubes (black),NaP_7 (blue), NaP_7@TiO_2 (red), **b)** TiO_2 (black), SnIP (blue), SnIP@TiO_2 (red), **c)** TiO_2 (black), $(CuI)_3P_{12}$ (blue), $(CuI)_3P_{12}$@TiO_2 (red) and Tauc plot for determination of optical band gap of **d)** TiO_2 (black), NaP_7 (blue), NaP_7@TiO_2 (red) **e)** TiO_2 (black), SnIP (blue), SnIP@TiO_2 (red), **f)** TiO_2 (black), $(CuI)_3P_{12}$ (red), $(CuI)_3P_{12}$@TiO_2 (blue). (CuIP ⇒ $(CuI)_{12}P_3$).

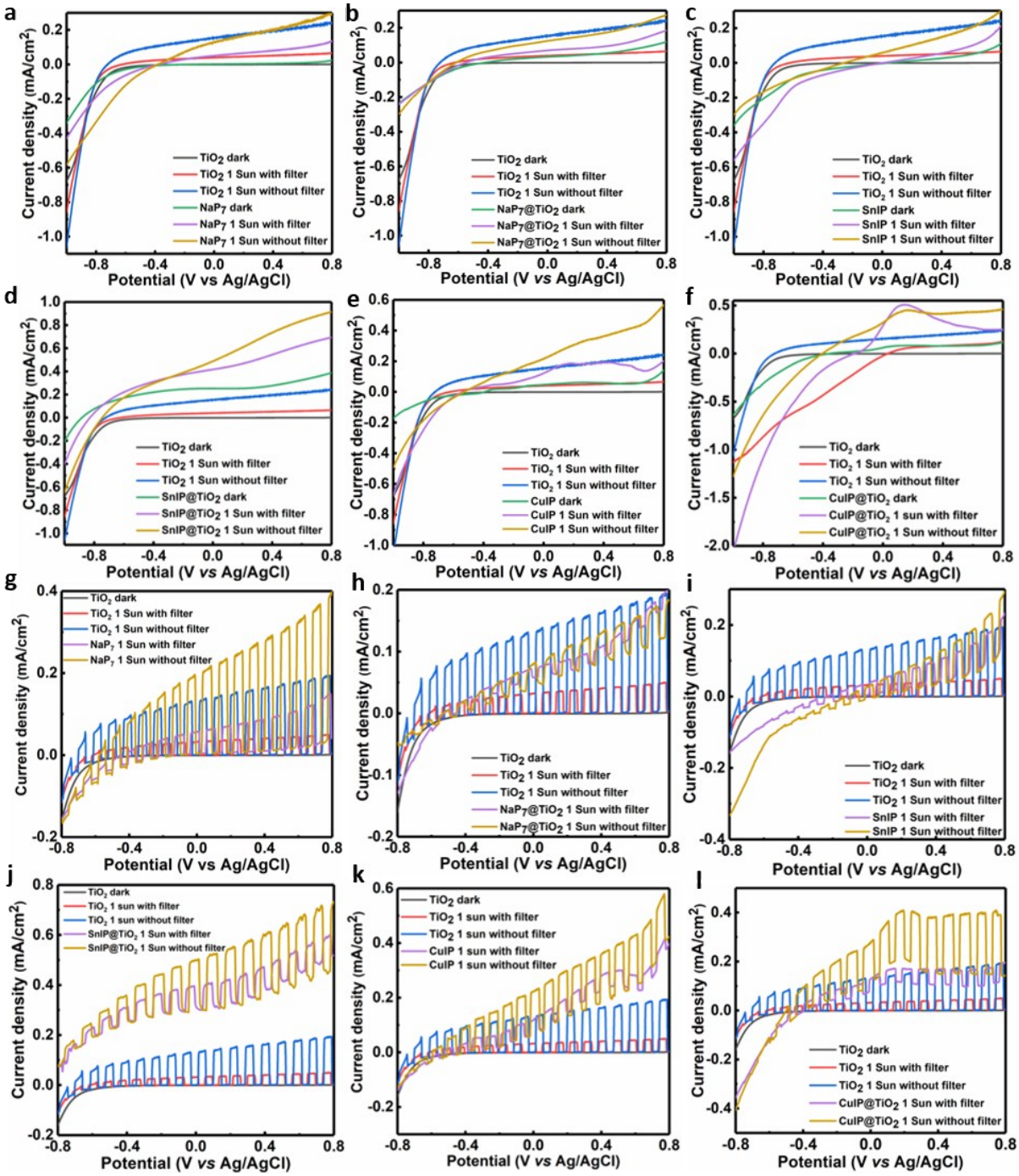

Figure S11. a) - l) Photocurrent density *vs* applied voltage plot with on-off cycles of TiO_2 nanotubes *vs* NaP_7, NaP_7@TiO_2, SnIP, SnIP@TiO_2, $(CuI)_3P_{12}$, $(CuI)_3P_{12}$@TiO_2. (CuIP ⇒ $(CuI)_{12}P_3$).

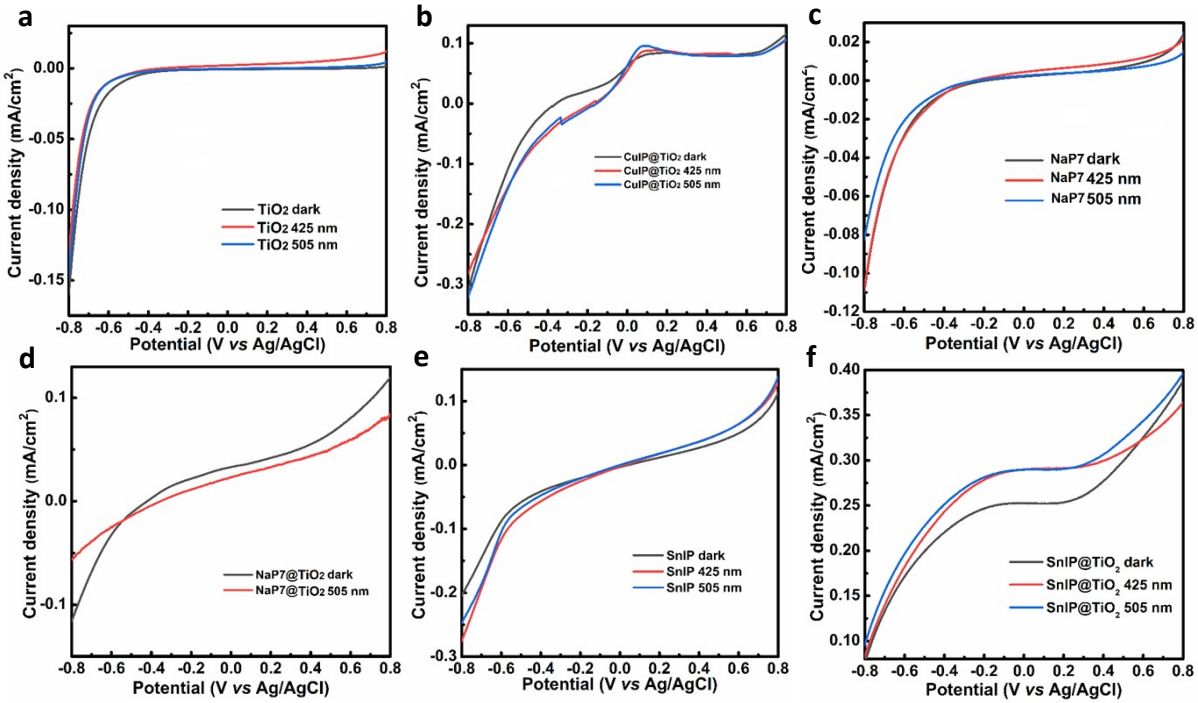

Figure S12. **a) – f)** Photocurrent density *vs* applied voltage plot of TiO_2 nanotubes, $(CuI)_3P_{12}$@TiO_2, NaP_7, NaP_7@TiO_2, SnIP and SnIP@TiO_2 under the illumination of LED 425 and 505 nm. (CuIP ⇒ $(CuI)_{12}P_3$).

Interface photon-to-current performance

Investigations on semiconductor/interface performance revealed following diagnostic efficiencies of the materials.[37, 38]

Applied bias photon-to-current efficiency (ABPE):

The applied bias photon-to-current efficiency percentage (ABPE%) which demonstrates photo-conversion efficiency under applied bias of the photoanode was determined by plotting a graph between ABPE% and applied voltage on RHE (reversible hydrogen electrode) scale. The ABPE% was calculated by using following expression:

$$\text{ABPE (\%)} = [J\ (\text{mA cm}^{-2}) \times (1.23 - V_b) / P\ (\text{mW cm}^{-2})] \times 100 \quad (1)$$

Where, J is the current density, V_b is the applied voltage at RHE scale and P is the power density of the incident light.

The applied voltage on Ag/AgCl scale was converted to RHE scale by using following expression.

$$V_{RHE} = V_{Ag/AgCl} + 0.059\ pH + V^0_{Ag/AgCl} \quad (2)$$

Where $V^0_{Ag/AgCl}$ = 0.197 V.

Incident photon-to-current efficiency (IPCE) also referred as external quantum efficiency (EQE):

The IPCE which is a measure of the obtained photocurrent (number of electrons collected) per incident photon flux as a function of wavelength was calculated at 0.6 V *vs* Ag/AgCl (1.23 V *vs* RHE, thermodynamic water splitting potential) by irradiating samples with a 505 nm wavelength LED (40.48 mW cm^{-2}). The IPCE values were calculated using the following expression.

$$\text{IPCE\%} = [1240 \times J\ (\text{mA cm}^{-2}) / \lambda\ (\text{nm}) \times P\ (\text{mW cm}^{-2})] \times 100 \quad (3)$$

Where, J is the photocurrent density, λ is the wavelength of incident light in nm, and P is the power density of the incident light.

Absorbed photon-to-current efficiency percentage (APCE%) also referred to as internal quantum efficiency (IQE):

Since IPCE is a measure to incident photons conversion efficiency, it doesn't take the loss of photons being unabsorbed by the materials into account. So, absorbed photon-to-current efficiency percentage (APCE%) which

define the photocurrent collected per incident photon absorbed is used to demonstrate device performances. The APCE% can be calculated by following formulas:

$$\text{APCE\%} = (\text{IPCE/LHE}) \times 100 \quad (4)$$

Where, *LHE* is the light harvesting efficiency or absorbance which is a number of electron-hole pairs produced as fraction per incident photon flux. By considering that each absorbed photon produces equal electron hole pairs, the value of LHE or absorptance calculated by Beer's law can be expressed by following equation.

LHE or absorptance = $(1\text{-}10^{-A})$

$$\text{APCE\%} = [1240 \times J\ (\text{mA cm}^{-2})/\lambda\ (\text{nm}) \times P\ (\text{mW cm}^{-2}) \times (1\text{-}10^{-A})] \times 100 \quad (5)$$

Where, J is photocurrent density, λ is wavelength of incident light in nm, P is the power density of incident light, *LHE* is light harvesting efficiency and A is absorbance at measured wavelength.

Semiconductor-electrolyte interface

Electrochemical impedance spectroscopy

Semiconductor electrolyte interfacial (SEI) behaviour of NaP_7 and NaP_7@TiO_2, SnIP, SnIP@TiO_2, $(CuI)_3P_{12}$, $(CuI)_3P_{12}$@TiO_2 were analysed using electrochemical impedance spectroscopy (EIS), whereby Nyquist plots were obtained, between frequencies of 1 and 10,000 Hz at -0.4 V vs Ag/AgCl, using dark and one-sun conditions. EIS Nyquist plots (Figure S13a, b and c) clearly indicate higher charge transfer resistance in dark conditions when compared to those in one-sun illumination condition. Equivalent circuit diagram representing the Nyquist plots is shown in Figure S13d, wherein in $\boldsymbol{R_S}$, $\boldsymbol{R_C}$, $\boldsymbol{R_T}$, $\boldsymbol{C_{SC}}$, and $\boldsymbol{C_H}$ are electrolyte resistance, charge transfer resistance, charge transport resistance, space charge capacitance, and electrochemical double-layer (Helmholtz) capacitance, respectively. $\boldsymbol{Q}$ is a constant phase element with coefficient $\boldsymbol{n}$. The values of circuit parameters are listed in Table S4. As obtained by equivalent circuit model, $\boldsymbol{R_C}$ was the same (i.e. 10 ohms) $(CuI)_3P_{12}$ and SnIP, as it was (i.e. 1 ohm) for SnIP@TiO_2 and NaP_7@TiO_2. RC for $(CuI)_3P_{12}$@TiO_2 and NaP_7 were rather high at 50 and 30 ohms, respectively. Calculated recombination lifetime (τ, using (6) values are listed in Table S5, and indicate reasonably long-lived holes for all samples, and particularly for SnIP and NaP_7.

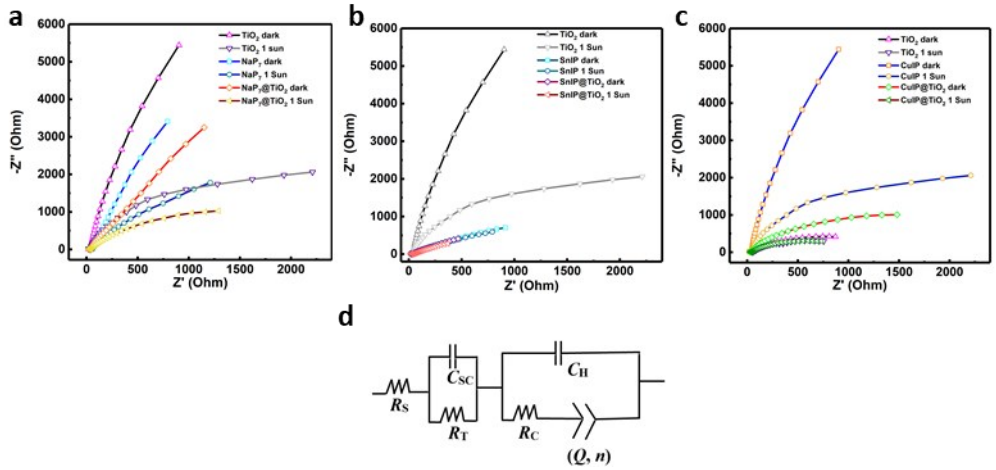

Figure S13. Nyquist plots measured in 0.1 M KOH, under dark conditions and AM1.5 G light irradiation (100 mW cm^{-2}) **a)** TiO_2 nanotubes (black and magenta), NaP_7 (light and dark blue), NaP_7@TiO_2 (light and dark red), **b)** TiO_2 (black and magenta), SnIP (dark and light green), SnIP@TiO_2 (light and dark red), **c)** TiO_2 (black and magenta), $(CuI)_3P_{12}$ (light and dark blue), $(CuI)_3P_{12}$@TiO_2 (light and dark red). **d)** Equivalent circuit diagram of the EIS Nyquist plots shown in a, b and c. (CuIP ⇒ $(CuI)_{12}P_3$).

$$\tau = R_T C_{SC} \quad (6)$$

$$\frac{1}{C_{SC}^2} = \frac{2}{\varepsilon_0 \varepsilon_r N_D}\left\{(V - V_{FB}) - \frac{kT}{e}\right\} \quad (7)$$

$$N_D = \frac{2}{\varepsilon_0 \varepsilon_r}\left\{\frac{dV}{dC_{SC}^2}\right\} \quad (8)$$

$$W = \{\frac{2\varphi\varepsilon_0\varepsilon_r}{eN_D}\}^{\mathfrak{G}} \quad (9)$$

Impedance-potential analysis

Further insights about SEI of the samples were gained *via* Mott Schottky's equations (eq. (7) and (8)), which were used to calculate charge carrier concentration (N_D), and flat band potential (V_{FB}). In eq. (7) and (8), C_{SC} is space-charge capacitance per unit area; ε_r the dielectric constant of the samples, which may be assumed to be 45, i.e. same as that of anatase TiO_2.[39, 40] N_D is carrier concentration; ε_0 is the vacuum permittivity (8.854 ×10^{-14} F cm^{-1}); k is the Boltzmann constant (1.381 ×10^{-23} J K^{-1}); ***T*** is the temperature in (298 K); ***e*** is the electron charge (1.602×10^{-19} C); V_{FB} is the flat band potential; and ***V*** is the applied potential. N_D, the charge carrier concentration, is calculated from the slope (term within the bracket in eq. (8) of the Mott Schottky's plots (Figure S14), using eq. (8). V_{FB}, is the point of intersection of the slope of the Mott Schottky's plot with the potential axis, as shown in Figure S14. N_D and V_{FB} of the samples are listed in Table S5. N_D of the order of 1020 cm^{-3}, is well known for anatase TiO_2[41] N_D of the composites of $(CuI)_3P_{12}$ and SnIP with TiO_2 decreased, as it did for bare $(CuI)_3P_{12}$ and SnIP, while that of NaP_7@TiO_2 increased slightly from bare TiO_2 nanotube arrays, while that for bare NaP_7 decreased slightly. Width of depletion layer, ***W***, is calculated using eq. (9) at 1.23 V *vs* RHE in eq. (9), where φ is the potential drop across the space layer. ***W*** is highest for SnIP and SnIP@TiO_2 indicating maximum band bending in those samples due to the lower carrier concentration.

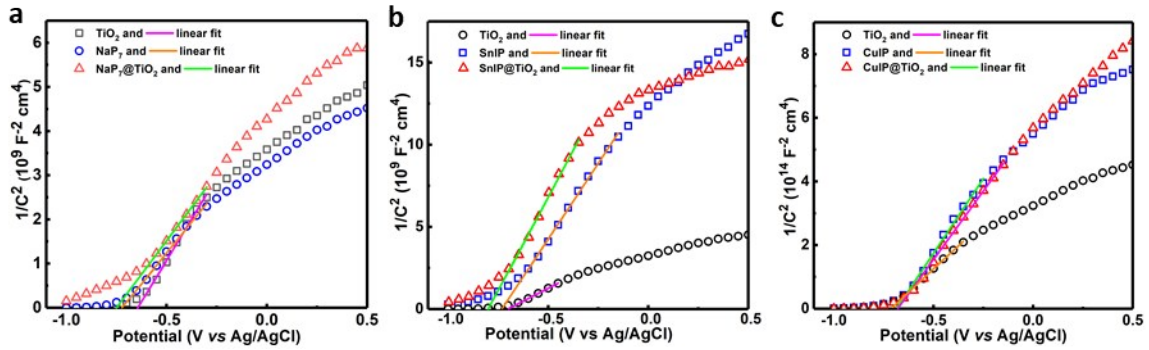

Figure S14. Mott-Schottky plots, linear fit of plot intersecting on abscissa reveal flat band potential of **a)** TiO_2 nanotubes (black), NaP_7 (blue), NaP_7@TiO_2 (red), **b)** TiO_2 (black), SnIP (blue), SnIP@TiO_2 (red), **c)** TiO_2 (black), $(CuI)_3P_{12}$ (blue), $(CuI)_3P_{12}$@TiO_2 (red) in 0.5 M Na_2SO_4. (CuIP ⇒ $(CuI)_{12}P_3$).

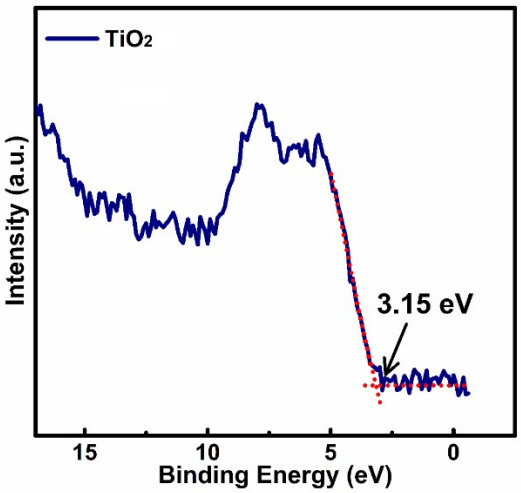

Figure S15. XPS valance band spectra of TiO_2 nanotube membranes showing the position of valance band maxima (VB_{max}) below Fermi level.

Kelvin Probe Force Microscopy (KPFM) Mesurement

To understand the dynamics of charge carrier separation and probe heterojunction formation between polyphosphides and TiO_2, surface potential (SP) difference of materials was determined using Kelvin Probe Force

Microscopy (KPFM) (Figure S16). The AFM topographical images of the samples displayed rough morphology and evidential presence of nanotube arrays (Figure S16a-d). The surface potential (SP) map of bare TiO_2, NaP_7@TiO_2, CuIP@TiO_2 and SnIP@TiO_2 deposited on FTO under dark condition is displayed in Figure S16a-d. The surface potential map of the samples shows uniform charge distribution at all sample surfaces. For bare TiO_2 nanotubes some bright region was observed which demonstrates electron rich surface of *n*-type TiO_2 nanotubes. Furthermore, the surface potential map contrast of SnIP@TiO_2 sample was slightly higher than other hybrid materials (NaP_7@TiO_2 and CuIP@TiO_2) which demonstrates higher electronic density of these materials. The surface potential distribution of bare TiO_2 was found to be ~38 mV, while SP of polyphosphide@TiO_2 hybrids, NaP_7@TiO_2, CuIP@TiO_2 and SnIP@TiO_2 was calculated to be ~ 27, 26, and 31 mV. A slightly negative shift of SP distribution of hybrid samples was corroborated to the lowering of work function value of nanohybrids. The lowering of WF (work function) value is attributed to the uplifting of the Fermi level of polyphosphides during Fermi level alignment in heterojunction formation because of charge carrier gradients (in-built electric field). The evident change in WF values and band structure clearly suggests successful formation of heterojunction between the materials.

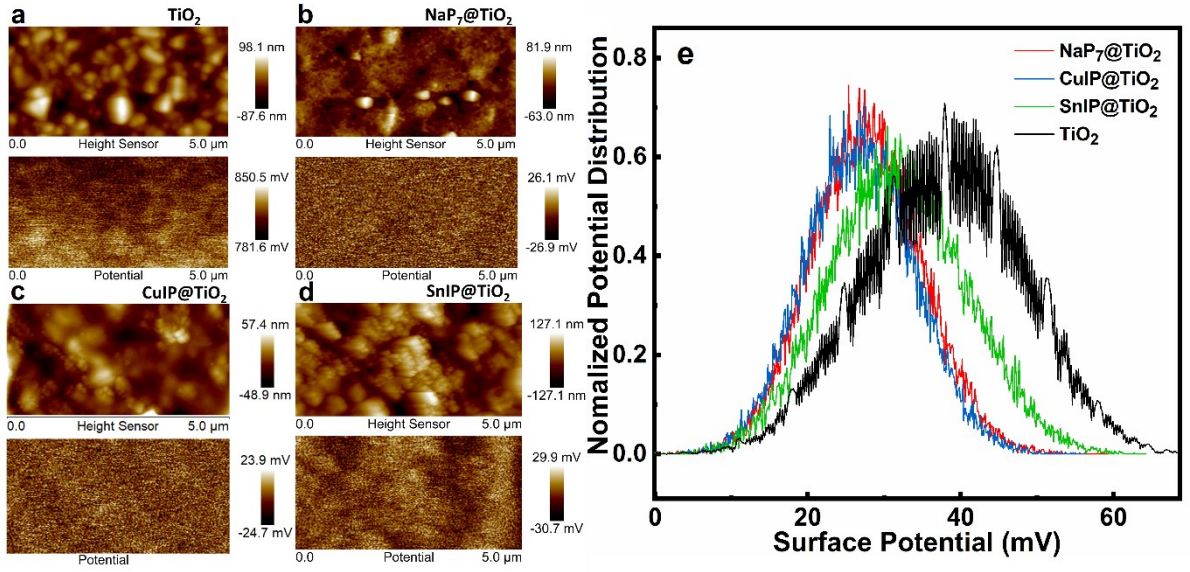

Figure S16. Topographical AFM images and surface potential map of **a)** TiO_2 nanotube, **b)** NaP_7@TiO_2, **c)** $(CuI)_3P_{12}$@TiO_2, **d)** SnIP@TiO_2 and **e)** surface potential distribution of bare TiO_2 nanotubes (black), NaP_7@TiO_2 (red), $(CuI)_3P_{12}$@TiO_2 (blue) and SnIP@TiO_2 (green) samples deposited on FTO under dark conditions.

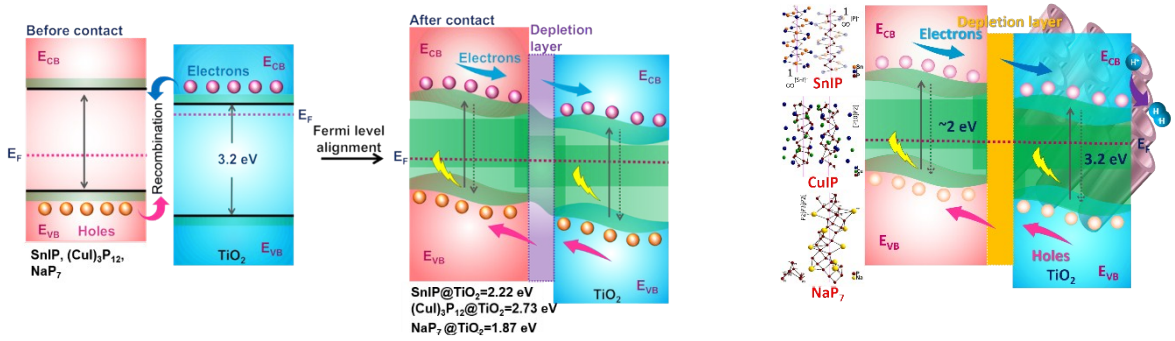

Figure S17. Left side: Plausible mechanism of charge separation in inorganic phosphides@TiO_2 heterojunction. Right side: Hybrid materials including heterojunction formation between TiO_2 nanotubes and different polyphosphides (NaP_7, SnIP and $(CuI)_3P_{12}$) for PEC-water-oxidation. (CuIP ⇒ $(CuI)_{12}P_3$).

EDS analysis

Table S1. Elemental analysis of deposited crystals found on both sides of the membranes and different spots along the razor cut cross section of NaP_x@TiO_2 membranes *via* EDS-measurements. Elemental composition in at.% with corresponding molar ratio deriving from the Na and P content and normalized to the Na content. Atomic percent of Ti is representing Ti in TiO_2.

EDS - NaP_x	**Na (at%)**	**P (at%)**	**Ti (at%)**	
NaP_7	12.5	87.5		NaP_7
NaP_{15}	6.25	93.75		NaP_{15}
NaP_7 measured, crystal	12.0(4)	87.9(1)	-	$Na_{0.96}P_{7.03}$
NaP_{15} measured, crystal	5.6(8)	94.4(2)	-	$Na_{0.9}P_{15.1}$
NaP_x@TiO_2 cross section 1	3.6(2)	16.4(2)	80.1(2)	$NaP_{4.5}$
NaP_x@TiO_2 cross section 2	1.5(1)	13.5(1)	85.0(3)	NaP_9

Table S2. Elemental analysis of deposited crystals found on both sides of the membranes and different spots along the razor cut cross section of SnIP@TiO_2 membranes *via* EDS-measurements. Elemental composition in at% with corresponding molar ratio deriving from the Sn, I and P content and normalized to the P content. Atomic percent of Ti is representing Ti in TiO_2.

EDS - SnIP	**Sn (at%)**	**I (a%)**	**P (at%)**	**Ti (at%)**	
SnIP	1	1	1		SnIP
SnIP measured, crystal	37.8(3)	26.3(3)	35.7(1)	-	$SnI_{0.7}P$
SnIP@TiO_2 cross section 1	13.2(2)	9.4(2)	20.2(2)	57.1(4)	$SnI_{0.7}P$
SnIP@TiO_2 cross section 2	10.5(6)	7.4(4)	18.6(8)	63.5(2)	$Sn_{0.6}I_{0.4}P$

Table S3. Elemental analysis of deposited crystals found on both sides of the membranes and different spots along the razor cut cross section of $(CuI)_3P_{12}$@TiO_2 membranes *via* EDS-measurements. Elemental composition in at% with corresponding molar ratio deriving from the Cu, I and P content and normalized to the P content. Atomic percent of Ti is representing Ti in TiO_2.

EDS - $(CuI)_3P_{12}$	**Cu (at%)**	**I (at%)**	**P (at%)**	**Ti (at%)**	
$CuI)_3P_{12}$	16.67	16.67	66.67		$Cu_3I_3P_{12}$
$(CuI)_3P_{12}$ measured, crystal	14.7(4)	16.1(3)	69.1(3)	-	$Cu_{2.6}I_{2.8}P_{12}$
$(CuI)_3P_{12}$@TiO_2 cross section 1	2.4(3)	2.5(3)	24.5(3)	72.6(5)	$Cu_{1.2}I_{1.2}P_{12}$
$(CuI)_3P_{12}$@TiO_2 cross section 2	16.5(5)	13.2(6)	69.0(5)	73.0(8)	$Cu_{2.9}I_{2.3}P_{12}$

Electrochemical impedance spectroscopy and impedance-potential analysis

Table S4. Values of electrolyte resistance R_S, charge transfer resistance R_C, charge transport resistance R_T, space charge capacitance C_{SC}, electrochemical double-layer (Helmholtz) capacitance C_H and constant phase element Q with coefficient n for $(CuI)_3P_{12}$, $(CuI)_3P_{12}$@TiO_2, SnIP, SnIP@TiO_2, NaP_7, NaP_7@TiO_2, obtained by fitting the Nyquist plots to the equivalent circuit (**Figure S13**).

Sample	R_S (Ohm)	C_{SC} (F)	R_T (Ohm)	C_H (F)	R_C (Ohm)	Q (Fs^{-1+n})	n
$(CuI)_3P_{12}$	16	9.00×10^{-8}	21	1.25×10^{-5}	10	5.50×10^{-4}	0.35
$(CuI)_3P_{12}$@TiO_2	16	6.00×10^{-8}	31	1.85×10^{-5}	50	5.80×10^{-4}	0.39
SnIP	16	1.00×10^{-7}	30	1.00×10^{-5}	10	4.75×10^{-4}	0.45
SnIP@TiO_2	16	1.10×10^{-7}	22	6.00×10^{-6}	1	9.50×10^{-4}	0.50
NaP_7	16	2.00×10^{-7}	16	1.50×10^{-5}	30	2.00×10^{-4}	0.54
NaP_7@TiO_2	16	8.50×10^{-8}	22	1.50×10^{-5}	1	2.10×10^{-4}	0.52

Table S5. Values of charge carrier concentration N_D, flat band potential V_{FB}, width of depletion layer W and calculated recombination lifetime τ for $(CuI)_3P_{12}$, $(CuI)_3P_{12}$@TiO_2, SnIP, SnIP@TiO_2, NaP_7, NaP_7@TiO_2 and TiO_2, obtained by fitting the Nyquist plots to the equivalent circuit (**Figure S13**).

Sample	N_D (cm^{-3})	V_{FB} (V *vs* Ag/AgCl)	V_{FB} (V *vs* NHE at pH-0)	W (nm)	τ (µs)
$(CuI)_3P_{12}$	3.88×10^{20}	-0.721	-0.522	113.18	1.90
$(CuI)_3P_{12}$@TiO_2	3.83×10^{20}	-0.692	-0.493	157.14	1.90
SnIP	1.69×10^{20}	-0.730	-0.531	712.80	3.00
SnIP@TiO_2	1.05×10^{20}	-1.930	-1.731	922.89	2.40
NaP_7	4.75×10^{20}	-0.670	-0.471	376.09	3.20
NaP_7@TiO_2	5.62×10^{20}	-0.780	-0.581	118.95	1.90
TiO_2	5.05×10^{20}	-0.702	-0.503	197.42	-

Table S6. Binding energies of different element and species present in TiO_2 nanotubes, NaP_7, NaP_7@TiO_2, $(CuI)_3P_{12}$, $(CuI)_3P_{12}$@TiO_2, SnIP, SnIP@TiO_2.

Sample	Ti2p ($Ti2p_{3/2}$) ($Ti2p_{1/2}$)	O1s ($O_{latt.}$) (-OH)	Na1s (Na1s)	Cu2p ($Cu\ 2p_{3/2}$) ($Cu2p_{1/2}$)	Sn3d ($Sn3d_{5/2}$) ($Sn3d_{3/2}$)	I3d ($I3d_{5/2}$) ($I3d_{3/2}$)	P2p ($P2p_{3/2}$) ($P2p_{1/2}$) (P_xO_y)
TiO_2	459.46 465.27	530.98 532.70	-	- -	- -	- -	- - -
NaP_7	- -	- -	1063.74	- -	- -	-	129.90 130.77 134.56
NaP_7@TiO_2	459.46 465.27	530.98 532.70	1071.83	- -	- -	-	130.00 130.98 133.82
$(CuI)_3P_{12}$	- -	- -	-	932.91 952.55	- -	619.94 631.42	134.39 135.27 -
$(CuI)_3P_{12}$@TiO_2	459.46 465.27	530.48 532.64	-	932.91 952.55	- -	620.30 631.89	134.40 135.33 -
SnIP	- -	- -	-	- -	487.51 495.88	619.87 631.37	133.73 134.71 139.77
SnIP@TiO_2	- -	530.98 532.74	-	- -	487.51 495.88	619.87 631.37	133.94 134.83 139.77

All binding energy values are in eV.

References

1. G. K. Mor, K. Shankar, M. Paulose, O. K. Varghese and C. A. Grimes, *Nano Lett.*, 2006, **6**, 215-218.
2. C. Grotz, M. Köpf, M. Baumgartner, L. A. Jantke, G. Raudaschl-Sieber, T. F. Fässler and T. Nilges, *Z. Anorg. Allg. Chem.*, 2015, **641**, 1395-1399.
3. D. Pfister, K. Schaefer, C. Ott, B. Gerke, R. Poettgen, O. Janka, M. Baumgartner, A. Efimova, A. Hohmann, P. Schmidt, S. Venkatachalam, L. van Wuellen, U. Schuermann, L. Kienle, V. Duppel, E. Parzinger, B. Miller, J. Becker, A. Holleitner, R. Weihrich and T. Nilges, *Adv. Mater. (Weinheim, Ger.)*, 2016, **28**, 9783-9791.
4. W. G. Palmer, *Experimental inorganic chemistry*, Cambridge University Press, Cambridge, 1962.
5. A. Pfitzner and E. Freudenthaler, *Angew. Chem. Int. Ed.*, 1995, **34**, 1647-1649.
6. U. K. Thakur, A. M. Askar, R. Kisslinger, B. D. Wiltshire, P. Kar and K. Shankar, *Nanotechnology*, 2017, **28**, 274001.
7. M. P. Baumgartner, Technische Universität München, 2017.
8. M. Baudler, *Angew. Chem.*, 1982, **94**, 520-539.
9. M. Baudler, *Angew. Chem.*, 1987, **99**, 429-451.
10. M. Baudler and K. Glinka, *Chem. Rev.*, 1993, **93**, 1623-1667.
11. S. Böcker and M. Häser, *Z. Anorg. Allg. Chem.*, 1995, **621**, 258-286.
12. G. Yang, D. Chen, H. Ding, J. Feng, J. Z. Zhang, Y. Zhu, S. Hamid and D. W. Bahnemann, *Appl. Catal. B*, 2017, **219**, 611-618.
13. M. Wang, B. Nie, K.-K. Yee, H. Bian, C. Lee, H. K. Lee, B. Zheng, J. Lu, L. Luo and Y. Y. Li, *Chem. Commun.*, 2016, **52**, 2988-2991.
14. W.-J. Kwak, Z. Chen, C. S. Yoon, J.-K. Lee, K. Amine and Y.-K. Sun, *Nano Energy*, 2015, **12**, 123-130.
15. T. Kajita and T. Itoh, *Phys. Chem. Chem. Phys.*, 2018, **20**, 2188-2195.
16. J. Song, C. Zhu, B. Z. Xu, S. Fu, M. H. Engelhard, R. Ye, D. Du, S. P. Beckman and Y. Lin, *Adv. Energy Mater.*, 2017, **7**, 1601555.
17. X. Zhong, Y. Jiang, X. Chen, L. Wang, G. Zhuang, X. Li and J.-g. Wang, *J. Mater. Chem. A*, 2016, **4**, 10575-10584.
18. Y. Zhou, C. Chen, N. Wang, Y. Li and H. Ding, *J. Phys. Chem. C*, 2016, **120**, 6116-6124.
19. R. Kumar, S. Govindarajan, R. K. Siri Kiran Janardhana, T. N. Rao, S. V. Joshi and S. Anandan, *ACS Appl. Mater. Interfaces*, 2016, **8**, 27642-27653.
20. F. Amano, M. Nakata, A. Yamamoto and T. Tanaka, *J. Phys. Chem. C*, 2016, **120**, 6467-6474.
21. I.-H. Tseng, W.-C. Chang and J. C. Wu, *Appl. Catal., B*, 2002, **37**, 37-48.
22. C. S. Chen, A. D. Handoko, J. H. Wan, L. Ma, D. Ren and B. S. Yeo, *Catal. Sci. Technol.*, 2015, **5**, 161-168.
23. C. S. Chen, J. H. Wan and B. S. Yeo, *J. Phys. Chem. C*, 2015, **119**, 26875-26882.
24. D. S. Bhachu, S. J. Moniz, S. Sathasivam, D. O. Scanlon, A. Walsh, S. M. Bawaked, M. Mokhtar, A. Y. Obaid, I. P. Parkin and J. Tang, *Chem. Sci.*, 2016, **7**, 4832-4841.
25. M. J. Islam, D. A. Reddy, N. S. Han, J. Choi, J. K. Song and T. K. Kim, *Phys. Chem. Chem. Phys.*, 2016, **18**, 24984-24993.
26. D. Hanlon, C. Backes, E. Doherty, C. S. Cucinotta, N. C. Berner, C. Boland, K. Lee, A. Harvey, P. Lynch and Z. Gholamvand, *Nat. Commun.*, 2015, **6**, 8563.
27. Z. Niu, J. Jiang and L. Ai, *Electrochem. Commun.*, 2015, **56**, 56-60.
28. G. G. Ninan, C. S. Kartha and K. Vijayakumar, *Sol. Energy Mater. Sol. Cells*, 2016, **157**, 229-233.
29. W. Gao, K. Zielinski, B. N. Drury, A. D. Carl and R. L. Grimm, *J. Phys. Chem. C*, 2018, **122**, 17882-17894.
30. M. Yan, Y. Hua, F. Zhu, W. Gu, J. Jiang, H. Shen and W. Shi, *Appl. Catal. B*, 2017, **202**, 518-527.
31. J. C.-R. Ke, D. J. Lewis, A. S. Walton, B. F. Spencer, P. O'Brien, A. G. Thomas and W. R. Flavell, *J. Mater. Chem. A*, 2018.
32. X.-D. Wang, Y.-F. Xu, H.-S. Rao, W.-J. Xu, H.-Y. Chen, W.-X. Zhang, D.-B. Kuang and C.-Y. Su, *Energy Environ. Sci.*, 2016, **9**, 1468-1475.
33. H. Tabassum, W. Guo, W. Meng, A. Mahmood, R. Zhao, Q. Wang and R. Zou, *Adv. Energy Mater.*, 2017, **7**, 1601671.
34. S. G. Ullattil and P. Periyat, *J. Mater. Chem. A*, 2016, **4**, 5854-5858.
35. H. Zhao, M. Wu, J. Liu, Z. Deng, Y. Li and B.-L. Su, *Appl. Catal. B*, 2016, **184**, 182-190.
36. M. S. Milien, U. Tottempudi, M. Son, M. Ue and B. L. Lucht, *J. Electrochem. Soc.*, 2016, **163**, A1369-A1372.
37. Z. Chen, H. N. Dinh and E. Miller, *Photoelectrochemical water splitting*, Springer, 2013.
38. X. Zhang, B. Zhang, K. Cao, J. Brillet, J. Chen, M. Wang and Y. Shen, *J. Mater. Chem. A*, 2015, **3**, 21630-21636.
39. H. Wang, Y. Liang, L. Liu, J. Hu and W. Cui, *J. Hazard. Mater.*, 2018, **344**, 369-380.
40. A. Muñoz, Q. Chen and P. Schmuki, *J. Solid State Electrochem.*, 2007, **11**, 1077-1084.
41. F. Y. Oliva, L. a. B. Avalle, E. Santos and O. R. Cámara, *J. Photochem. Photobiol., A*, 2002, **146**, 175-188.